Higher-order hub cells involved in feedforward motifs as critical factors in epileptic network instability

Darian Hadjiabadi[1,2,*], Matthew Lovett-Barron[1,3], Ivan Raikov[2], Fraser Sparks[4,5,6], Zhenrui Liao[4,5,6], Scott C. Baraban[7], Jure Leskovec[8], Attila Losonczy[4,5,6], Karl Deisseroth[1,9], Ivan Soltesz[2]

[1] Department of Bioengineering, Stanford University, Stanford, CA, USA
[2] Department of Neurosurgery, Stanford University, Stanford, CA, USA
[3]Neurobiology Section, Division of Biological Sciences, University of California San Diego, La Jolla, CA, USA
[4]Department of Neuroscience, Columbia University, New York, NY, USA
[5]Mortimer B. Zuckerman Mind Brain Behavior Institute, Columbia University, New York, NY, USA
[6]The Kavli Institute for Brain Science, Columbia University, New York, NY, USA
[7]Department of Neurological Sciences, University of California San Francisco, San Francisco, CA, USA
[8]Department of Computer Science, Stanford University, Stanford, CA, USA
[9]Howard Hughes Medical Institute, Stanford University, Stanford, CA, USA

***** Corresponding author: Darian Hadjiabadi - dhh@stanford.edu

Highlights

- Whole brain single-cell calcium imaging in zebrafish combined with effective connectivity modeling was used to study epileptic network instability
- Preseizure whole brain networks were more sensitive to simulated targeted perturbation of single richly connected “hub” neurons
- Higher-order graph clustering revealed overexpression of a class of hub cells engaged in feedforward motifs in the unstable preseizure state
- Such higher-order hub neurons enhanced downstream excitation and were causally linked to network instability
- Higher-order hub cells were identified in the hippocampus of chronically epileptic mice, showing similar findings across models and species.

Abstract

Sixty-five million people suffer from epilepsy and associated cognitive decline worldwide. Therefore, there is urgent need to identify novel mechanisms involved in epileptic network instability. Densely connected “hub” neurons have been implicated as key controllers of developmental as well as epileptic circuits. While such hub cells are traditionally defined by connection count, how these connections contribute to interictal dynamics is not understood. We performed whole-brain single-cell calcium imaging of the larval zebrafish brain in an acute seizure model. Biologically constrained modeling of cell-cell effective interactions successfully reproduced experimental calcium dynamics and enabled hub identification. Simulated perturbation of single hub neurons in the preseizure state confirmed that such traditional hub cells can exert major influence over global dynamics. Novel higher-order graph analytics revealed that the sensitivity to perturbation is not simply linked to outgoing degrees but rather to overexpression of feedforward motifs surrounding the hub cells that enhance downstream excitation. Model- and species similarity of the key findings was supported by similar results from the hippocampus of chronically epileptic mice. Collectively, these data identify a specific class of high-order hub neuron that is richly involved in feedforward motifs as an attractive new target for seizure control.

Keywords: epilepsy; calcium imaging; effective connectivity; hub neurons; motifs

Introduction

Epileptic seizures are characterized by abnormal neural activity and synchronization across brain regions. Because substantial patient populations have medically uncontrolled seizures and suffer from comorbidities, significant research efforts have been directed at identifying novel features of interictal (i.e., in-between seizure episodes) activity that may offer new mechanistic targets for seizure control[1–3]. To date, studies employing unit recordings[4,5] and single-cell calcium imaging[6–8] have discovered core features of epileptic networks that cannot be inferred from populations recordings[9]. However, the underlying network principles of cell-cell communication that are essential for pathological seizure dynamics to emerge remain poorly understood.

Hub neurons orchestrate network synchrony in the healthy brain[10] and are implicated in seizure initiation[11,12]. Recent evidence in preseizure networks reported increased sensitivity to perturbation, suggesting that these networks are unstable[13]. However, the specific questions of whether hub neurons destabilize epileptic networks and what underlying changes to cell-cell communication networks enable this remain open. The role of hubs has only been elucidated in very specific brain regions and under relatively restricted imaging windows, presenting two significant technical and interpretation challenges. First, hub neurons are per definition a sparse cell population[10] and therefore their identification ideally should rely on large-scale imaging approaches. Second, epilepsy is a disorder involving widespread brain networks[14,15], therefore, performing analysis in only a specific brain region limits the interpretation of the data to exclude potential external sources that drive network activity.

To address these issues, we turned to larval zebrafish, whose optical transparency and small brain size (~100,000 neurons) have recently enabled unprecedented access to whole-brain neural activity at cellular resolution[16]. The usefulness of zebrafish in epilepsy research is highlighted by a neuromodulatory circuitry shared with mammals[17], high degree of genetic overlap with humans enabling translation[18,19], and agreement across single-cell studies with rodents[6–8]. Furthermore, effective connectivity modeling, which measures the causal influence of one entity against another, has been used to evaluate how macroscale brain regions communicate during the seizure state in larval zebrafish[20]. Such modeling approaches offer an opportunity to infer the underlying cell-cell effective connectivity (i.e. communication network) in control and preseizure brains, partially overcoming current technical limitations in measuring synaptic strengths over large-scale neural populations. The inferred connectivity matrix can subsequently be used to identify hub neurons, and controlled perturbation simulations of hubs can be systematically executed. Furthermore, modern network science tools can be applied to investigate the inferred communication network for critical features that reveal changes to network function.

Here, we systematically investigated the specific changes to cell-cell communication networks that enable hub neurons to destabilize epileptic networks. We deployed whole-brain cellular resolution calcium imaging to capture neural dynamics in larval zebrafish pentylenetetrazol (PTZ; a $GABA_A$ receptor antagonist) model of acute seizures[21]. The underlying cellular-resolution effective connectivity networks were inferred for both baseline and preseizure neural dynamics using chaotic recurrent neural networks[22]. Importantly, these models were biologically constrained for the first time to the zebrafish neuroanatomical connectome[23]. Richly connected traditional hubs were identified and computational simulations revealed that perturbation of a single hub in the preseizure brain induces significant changes in global network dynamics compared to control. Using higher-order clustering[24] on the learned connectivity matrix, we discovered that network stability is not causally linked to number of outgoing connections but rather to feedforward motifs surrounding hubs that enhance downstream excitation. Strategically disconnecting a fraction of ‘higher-order hubs’ from involvement in feedforward motifs stabilized networks to perturbation. Critically, similar results were found in chronically epileptic mice compared to control, indicating that our key findings hold in the mammalian brain and in a model of chronic temporal lobe epilepsy (TLE), the most common epilepsy in adults with over a third of patients lacking effective seizure control. Collectively, these results identify the emergence of ‘higher-order hubs’ as a new feature of network reorganization and as a key step in the destabilization of epileptic circuits.

Results

Whole brain imaging of larval zebrafish acute seizure model at single cell resolution

Whole brain larval zebrafish (*Tg(elavl3*:*H2B-GCaMP6s);* N=3) imaging was performed with volumetric two-photon microscopy for 25 minutes at 2Hz capture rate (**Fig 1A**, see Methods). Five minutes of baseline data was recorded for each fish followed by 15 mM PTZ[8,21] bath application. Each fish exhibited at least one seizure prior to cessation of imaging (see below). LFP recording was not included as previous studies have shown robust correlation between calcium signal and field potentials in PTZ model[8]. Anatomical volume stacks were registered and neural somata (**Fig 1B**) were extracted with methods used in[17]. We extracted fluorescence time series from 5000-7000 active neurons per fish across all major brain regions (**Fig 1C**).

The start of the preseizure state was defined as 1 minute after PTZ is introduced to account for transient activity. Seizure initiation was defined as three standard deviations above population mean calcium signal during baseline (pre-PTZ) and termination was defined as when the population mean signal dropped below this threshold. In agreement with prior literature[8], calcium dynamics within detected seizure period lasted 35-40 seconds and displayed significantly higher synchronicity (i.e. hypersynchronous state) compared to baseline (one-sided paired t-test, p=0.034 after Bonferroni correction) and preseizure (one-sided paired t-test, p=0.006 after Bonferroni correction) epochs (**Figs 1D,E**). For this work, we will be modeling baseline and preseizure calcium dynamics (**Fig 1F**), and we will not be focusing on seizure or post-seizure periods.

Cellular resolution effective connectivity modeling to infer cell-cell communication networks

We performed effective connectivity modeling of baseline and preseizure calcium dynamics (**Fig 1F**) to infer cell-cell communication networks. Modeling was undertaken with chaotic recurrent neural networks (RNN)[22] (**Fig 2A**, see Methods), which has previously been successful in fitting cellular-resolution calcium dynamics in the zebrafish[25]. The initially random connectivity structure of the chaotic RNN yields a balanced network that can be modified to match neural dynamics, and contrasts with networks specifically designed for a task. Each neuron imaged experimentally is represented by a node in the model. The parameters of the model are the synaptic connections between nodes, which can be interpreted as how much causal influence a source has on its target over a sub-second temporal window and can vary in sign and magnitude. The spontaneous and self-perpetuating chaotic dynamics were controlled through FORCE learning[26] (Methods), which uses a recursive-least square learning-rule on the connectivity parameters to reproduce a specified target output **(Fig 2C)**.

Here, we set target outputs to be the experimentally acquired calcium dynamics. We furthermore employed a 10% sparsity constraint ($\frac{N*(N-1)}{10}$ total parameters) to match reported connectivity patterns[27] and to prevent overfitting. While there may be many local minima for which the optimized parameters generate target calcium dynamics, one major issue is whether such inferences are realistic given the underlying neuroanatomy. To mitigate this, we constrained the optimization procedure using the known zebrafish structural connectome (S^{Macro})[23] (**Fig 2B**, Methods). Specifically, as previously described[23], S_{ij}^{Macro} is the sum of all neurite processes (axons and/or dendrites) inside regions *i* and *j* from neurons that project neurites to both regions, normalized by region volumes. In the optimization procedure, weights are adjusted proportional to how strongly connected the regions in which the source soma and target soma inhabit (**Fig 2C**).

Training incorporated two phases (**Fig 2C**). First, connectivity parameters were inferred for baseline calcium dynamics. After learning had converged, we identified the best fit baseline model and used that as the seed for learning preseizure calcium dynamics. In this regime, we can begin to untangle the cell-cell effective rewiring that takes place as a result of PTZ bath wash-in. For consistency, this was repeated three times with different initial conditions for each fish. Models converged for both baseline and preseizure state and FORCE learning captured both the global population and individual calcium dynamics during both brain states (**Fig 2D,** note scale bars).

Community detection (Methods) on the inferred parameter matrix identified relevant macroscale anatomical structures which were not observed in models training without the zebrafish structural connectome (**Supplementary Figure 1**). We validated that model dynamics were primarily driven by synaptic transmission and not noise (**Supplementary Figures 2A,B**). Furthermore, we found that outgoing inhibition per neuron decreased by 33% on average after PTZ bath wash-in (**Supplementary Figure 2C**), consistent with PTZ reducing $GABA_A$ receptor mediated inhibitory conductances[28].

Identification of outgoing and incoming traditional hubs

Traditional (i.e., connection-based; also known as degree- or edge-based) hub neurons were segregated into two classes: incoming and outgoing (**Fig 3A**). Outgoing hubs project while incoming hubs receive numerous strong connections. The optimized parameter matrix was binarized by keeping only the strongest excitatory connections (top 10%; **Fig 3B**). Degree distributions for both hub subtypes and across brain states displayed heavy-tailed distributions as reported experimentally[10] (**Fig 3C**). To identify outgoing and incoming hubs, the 90th percentile cutoff was calculated (i.e., hubs were defined as the 10% most connected cells; note that changing the 90% cutoff to a different percentile did not alter the key findings, see below). Cutoff values were independently calculated for incoming and outgoing hubs and between baseline and preseizure distributions (**Fig 3C**).

Importantly, outgoing and incoming hub cutoff threshold, and mean outgoing (incoming) degree of outgoing (incoming) hubs were not statistically different (two-sided unpaired t-test, $p>0.05$) between baseline and preseizure states (**Fig 3D**). There was approximately a 5% difference in the average outgoing (incoming) degree of outgoing (incoming) hubs between baseline and preseizure networks (**Fig 3D**). The spatial locations of outgoing and incoming hub neurons were visualized in the zebrafish anatomy for both baseline and preseizure networks (**Fig 3E**)**.** Outgoing hubs were primarily located in diencephalon and incoming hubs were primarily located in mesencephalon and telencephalon **(Fig 3F)**. PTZ did not cause significant changes in the macroscale anatomical locations of outgoing and incoming hubs **(Fig 3F)** (two-sided unpaired t-test, $p>0.05$).

Perturbation of individual outgoing hubs destabilize preseizure networks

Chaotic recurrent neural networks are a generative model and can therefore create new data instances. This property enabled us to generate synthetic calcium traces for each cell and therefore we tested the hypothesis that preseizure networks are more sensitive to perturbation of a single hub neuron compared to baseline networks. Briefly, the simulated perturbations involved 500 ms depolarizing current injection into a single hub neuron after 20% of epoch duration had elapsed. Initial analysis revealed that these depolarizations increased activity in neurons receiving strong excitatory inputs from the perturbed hub, and that this increase was higher in preseizure state than baseline state (**Supplementary Figures 3A,B**). Considering this, we therefore quantified the effect of perturbation on global network dynamics. Specifically, we measured the 'trajectory deviation' between the mean population calcium signal of the unperturbed network with the mean population calcium signal of the perturbed network. Trajectory deviation was calculated as the Euclidean distance between signals normalized by the number of time points until cessation of epoch.

The data reveal that depolarizing a single outgoing hub in the preseizure state caused significant deviation (one-sided Mann-Whitney U-test. $p<0.001$) in global dynamics (**Fig 4B,C**) compared to equivalent simulations in baseline networks (**Figs 4A,C**). Depolarizing incoming hubs (**Supplementary Figures 3C,D, Fig 4C**) and non-hubs (**Supplementary Figures 3C,D**) had significantly less influence in both networks. However, the trajectory deviation was higher when perturbing incoming hubs in the preseizure network compared to baseline (one-sided Mann-Whitney U-test, $p<0.001$) (**Fig 4C**). Therefore, the median trajectory deviation for incoming hubs was used to normalize against the trajectory deviation quantified from perturbation of single outgoing hubs.

While perturbing a single outgoing hub in baseline networks did have consequences on global dynamics as would be expected experimentally[10], perturbation of a single outgoing hub in the preseizure state altered global

dynamics more significantly (one-sided Mann-Whitney U-test, p<0.001) (**Fig 4D**). These findings were confirmed in all three imaged and modeled fish (one-sided paired t-test, p=0.041) (**Fig 4E**). Taken together, these data suggest that preseizure networks are more sensitive to perturbations and that even a single outgoing hub neuron can significantly influence global dynamics.

Visualizing connections between outgoing and incoming hubs

As reported above, PTZ bath wash-in did not significantly change several parameters associated with the outgoing and incoming degree distributions (**Figs 3C,D**) and did not significantly reorganize which macroscale anatomical regions the hub cells occupied (**Figs 3E,F**). Therefore, we hypothesized that nuanced rewiring of microcircuit effective connectivity patterns may be critical for understanding increase sensitivity to perturbation (**Fig 4**). We visualized the connectivity patterns between outgoing and incoming hubs for baseline (**Fig 4F**) and preseizure (**Fig 4G**) networks using force-directed graphs (Methods). Importantly, nodes clustered in force-directed graphs are highly connected. We observed increased number of outgoing – outgoing hub connections (**Fig 4G**, note golden edges forming a 'core') in preseizure networks compared to pre-PTZ baseline control.

Enhanced recurrent connectivity between outgoing hub neurons in preseizure networks suggest an important role for motifs. Motifs are subgraphs that are thought to provide insight on the functional properties of complex systems. Importantly, both structural and functional motifs have been implicated as essential building blocks for ensuring efficient neural computations[29]. In baseline toy model (**Fig 4H**, **top**), there is a single connection between outgoing hubs. Additionally, there are two feedforward motifs that are present in this network. Based on observations in **Fig 4G**, there are more connections between outgoing hubs. Therefore, preseizure toy model (**Fig 4H**, **bottom**) includes an additional connection between outgoing hubs 2 and 3. As a result of adding a single connection, there are now four feedforward motifs present in the network. Therefore, we hypothesized that the multiplicative emergence of feedforward motifs may be a core feature of cell-cell communication networks that destabilize the preseizure brain.

Emergence of higher-order hubs in the preseizure brain

Graph clustering is an intuitive method to isolate groups of nodes in a network that form numerous intra-group connections. Specifically, we identified 'higher-order' hubs using a higher-order clustering concept. The inputs to the algorithm were the directed binarized graph (**Fig 3B**), a motif *M*, and an individual outgoing hub identified in **Fig 3C** (i.e. the seed). The algorithm finds an optimal cluster surrounding the seed that rich in *M* with run-time that is invariant of the graph size (**Fig 5A, left**). More traditional edge clustering, which only considers simple edges, was also performed as a control (**Fig 5A, right**).

To stratify the importance of higher-order hubs on 'network influence', we first note that identified higher-order clusters are not isolated from the network. The quality of a higher-order cluster can be quantified using the motif conductance metric (**Fig 5B**). Generally speaking, conductance is a normalized measure that describes how much information or activity propagates to the rest of the network. Intuitively, higher conductance implies excitation propagates through the rest of the network more easily and furthermore indicates a poor cluster. Whereas traditional edge clustering only considers edges when calculating conductance, higher-order clustering considers motif instances (**Fig 5B**). Optimal clusters (i.e. minimal conductance) were identified for outgoing hubs in baseline and preseizure networks using the Motif-based Approximate Personalized PageRank (MAPPR) algorithm[24].

The data show that both edge conductance (individual: one-sided Mann-Whitney U-test, p<0.001; group: one-sided paired t-test, p=0.011) and feedforward motif conductance (individual: one-sided Mann-Whitney U-test, p<0.001; group: one-sided paired t-test, p=0.033) were elevated in preseizure networks (**Figs 5C,D**). However, the increase in feedforward motif conductance relative to baseline was significantly higher (one-sided paired t-test, p=0.047) than edge conductance (51.8% vs 2.4%; **Fig 5E**). We performed higher-order clustering on additional motifs, such as cycles, but found very few instances. Therefore, by looking at feedforward motif patterns that emerge during PTZ induced rewiring of cell-cell communication networks, we discovered that

higher-order hubs in preseizure networks allow excitation to propagate more readily to the rest of the network. Importantly, both individually (baseline Spearman's rho=-0.005, p>0.05; preseizure Spearman's rho=0.054, p>0.05) and as a group (unpaired two-sided t-test, p>0.05), feedforward motif conductance was not correlated to outgoing degree of the outgoing hub (**Fig 5F**), suggesting that the microcircuit features of an unstable network could not be deduced from looking at simple edges/connections alone.

Disconnecting higher-order hubs stabilizes preseizure networks

Our evidence so far suggests a correlation between two findings: 1) Perturbation of a single outgoing hub in preseizure networks has significant influence on global network dynamics, as quantified by trajectory deviation; 2) Higher-order hubs in preseizure networks are able to propagate excitatory activity to the rest of the network more easily, as quantified by feedforward motif conductance. To establish a causal link, we performed three computational experiments.

To compare the role of feedforward motifs versus simple edges on network function, we tested the hypothesis that reducing excitatory output from higher-order hubs will influence global network activity more than reducing excitatory output from a traditional hub. This was performed by uniformly dampening edges that projected from outgoing hubs and targeted neurons in its local higher-order cluster (for higher-order hubs) or its local edge cluster (for traditional hubs) by a dampening factor ranging from 0 to 1 (**Fig 6A**). A dampening factor of 1 implies no change to edge weight while a dampening factor of 0 effectively disconnects the outgoing hub from activating its local cluster. Results confirm that dampening the outputs of outgoing hubs to their respective higher-order cluster has greater effect on network activity in both baseline and preseizure networks (**Fig 6B, left**). However, this effect was more pronounced for preseizure state (**Fig 6B, right**).

Second, we tested the hypothesis that higher-order hubs with the highest motif-conductance (i.e. could propagate activity downrange more easily) have greater influence over network dynamics than higher-order hubs with low network conductance. To test this, higher-order hubs in preseizure network were ranked based on their feedforward motif conductance score and split into either top half or bottom half. Within each half, an equivalent fraction of higher-order clusters was disconnected from the network (**Fig 6C**; dampening factor = 0.0). As expected, simulations showed that disconnecting higher-order hubs with the highest conductance was effective in changing global network activity (**Fig 6D, top**). Interestingly, this effect was observed despite more edges being removed in the bottom half group (**Fig 6D, bottom**), and in total represented less than 0.1% of all edges in the network. Brute force disconnecting hubs with the highest outgoing degree (without taking local edge cluster into account) did not alter global network dynamics (**Fig 6D, top**). Lastly, higher-order hubs with highest conductance displayed increasing activity in between high calcium events compared to the remaining higher-order hub population (**Fig 6E**, note numbers) and were not biased towards having the highest outgoing degree values (one-sided KS test. p>0.05) (**Fig 6F**). Through this experiment, we showed that motif conductance gives important insight on network function and that this insight could not have been revealed through mining the network for simple edges.

Third, we tested the hypothesis that disconnecting higher-order hubs with the highest conductance rendered the network more stable to perturbation. Based on results from **Fig 6D** (top), higher-order hubs with the highest 37.5% feedforward motif conductance scores were disconnected. Spectrogram analysis reveal that overall oscillatory power was dampened uniformly over all frequency bands for most measured time periods (**Fig 6G**). Furthermore, we tracked the variance (i.e. total power) of the population mean calcium signal before and after perturbation of a single outgoing hub. As expected, the percent change in signal variance of the fully connected preseizure network was significantly higher than baseline network (39.8% to 69.1%; one-sided Mann-Whitney U-test, p<0.001 after Bonferroni correction). Disconnecting high-conductance higher-order hubs from the preseizure network significantly reduced signal variance from 69.1% to 31.7% (one-sided Wilcoxon signed-rank test, p<0.001 after Bonferroni correction) (**Fig 6H, left**). Furthermore, percent change in signal variance in response to perturbation of the disconnected network was not significantly different compared to baseline network (two-sided Mann-Whitney U-test, p=0.81 after Bonferroni correction) (**Fig 6H, left**), evidence

of renormalization. Additionally, disconnecting high-conductance higher-order hubs significantly decreased the trajectory deviation of global network activity compared to fully connected preseizure network (one-sided Wilcoxon signed-rank test, $p<0.001$) (**Figs 6H,I**). As a control (**Supplementary Figure 4**), disconnecting high-conductance hubs reduced the percent change in signal variance as a response to perturbation more significantly than either disconnecting the same number of hubs randomly (31.7% versus 99.8%, one-sided Wilcoxon signed-rank test, $p<0.001$) or the same number of low-conductance hubs (31.7% versus 67.6%; one-sided Wilcoxon signed-rank test, $p<0.001$).

Therefore, the network is more resilient to perturbation when disconnecting high conductance higher-order hubs. Taken together, these three computational experiments reveal that the microcircuit connectivity architecture surrounding hub neurons is a critical novel feature of stability in epileptic networks.

Higher-order hubs in mouse model of chronic temporal lobe epilepsy

We performed the same analysis in healthy control (N=3) and epileptic mice (intrahippocampal KA model; N=3) to address the question of whether our key findings above from the fish brain in an acute seizure model were overall consistent with what could be observed in a mammalian brain circuit in a chronic model of TLE, the most prevalent form of epilepsy in adults. Mice expressed GCaMP6f in dorsal dentate gyrus (DG) and the epileptic group had kainic acid (KA) injected unilaterally into ipsilateral ventral hippocampus. KA injected mice were monitored with video-EEG until emergence of spontaneous seizures. 2p calcium imaging of DG granule cells was performed in healthy mice and in chronically epileptic mice (**Figs 7A,B**, note differences in vertical axis of scale bars).

Granule cell calcium dynamics were modeled in healthy control mice and in chronically epileptic mice (600-800 neurons/mouse; 3-5 minute window) using chaotic recurrent neural networks (**Fig 7C**), as was done in zebrafish. Despite fewer neurons imaged in mouse dentate gyrus than in whole-brain of zebrafish, models for mouse data converged under a 40% sparsity constraint. Incoming and outgoing traditional hubs were identified with the method used in zebrafish (**Fig 7D**). Perturbation of a single outgoing hub in modeled control dentate network produced a transient deviation in global population dynamics but eventually returned to baseline levels (**Fig 7E, left**). In contrast, perturbation of a single outgoing hubs in modeled chronically epileptic dentate network resulted in significant trajectory deviation (**Fig 7E, right**). Control dentate networks were more resistant to perturbation of a single outgoing hub than chronically epileptic dentate networks as quantified by trajectory deviation (**Fig 7F**). Additionally, trajectory deviation in response to single outgoing hub perturbation was significantly higher than single incoming hub perturbation (one-sided Mann-Whitney U-test, $p<0.001$) for both networks (**Supplementary Figures 5A,B**).

The capacity for higher-order hubs to facilitate downstream excitation in TLE was studied next. Specifically, feedforward motif conductance of local higher-order clusters seeded on outgoing hubs was significantly higher (one-sided unpaired t-test, $p=0.0034$) in chronically epileptic dentate networks compared to control dentate networks (**Figs 7G,H**). Feedforward motif conductance was not correlated to outgoing degree (Spearman's rho=0.10, $p>0.05$) (**Fig 7I**) and top high conductance higher-order hubs was not biased towards the highest outgoing degree values (one-sided KS test, $p>0.05$) (**Fig 7J**). Disconnecting higher-order hubs with the top 20% highest feedforward conductance in chronically epileptic dentate networks led to a more stable network. Specifically, disconnection significantly reduced (one-sided Wilcoxon signed-rank test, $p<0.001$) global network trajectory deviation in response to single hub perturbation (**Supplementary Figure 5C**). Furthermore, disconnection significantly reduced (one-sided Wilcoxon signed-rank test, $p<0.001$) the change in global network signal variance in response to single hub perturbation (**Fig 7K**). This reduction was more significant compared to disconnecting the same number of random hubs (one-sided Wilcoxon signed-rank test, $p=0.0077$) or low-conductance hubs (one-sided Wilcoxon signed-rank test, $p=0.0024$) (**Supplementary Figures 5D,E**). Example traces of global network dynamics from TLE network in response to perturbation of the same hub before and after disconnecting high-conductance higher-order hubs are presented in **Fig 7L**.

These similar findings across both acute seizure model in zebrafish and in chronically epileptic mice suggest that the emergence of 'higher-order hubs' is a core principle of network reorganization that may be a key feature contributing to the destabilization of the epileptic brain.

Discussion

Here, we addressed the critical question of what network features enable hub neurons to destabilize epileptic networks. Our work took place in four stages: 1) Imaged whole larval zebrafish brain at cellular resolution; 2) Built for the first time biologically constrained models of experimentally acquired neural dynamics using chaotic recurrent neural network architecture and optimized with FORCE; 3) Mined hub neurons inferred from FORCE learning using novel higher-order clustering; 4) performed perturbation simulations of whole-brain dynamics at cellular resolution. Through rigorous quantification, we discovered that previously unrecognized 'higher-order' hub neurons involved in feedforward motifs play a critical role in destabilizing epileptic networks. This cellular-scale network reorganization was also found to be implicated in the dentate gyrus of chronically epileptic mice. Collectively, these data identify a specific class of high-order hub neuron that is an attractive new target for seizure control.

Modeling cell-cell interactions across the whole brain

Chaotic recurrent neural networks[22] and FORCE optimization[26] techniques have proven to be an effective tool for modeling neural dynamics and yielded insight on various topics such as hippocampal sequence generation[30], motor planning[31], and coping[25]. The underlying theoretical assumption is that the brain operates in a chaotic regime and evidence has shown that pathological conditions such as epilepsy can reduce this chaotic dimensionality[32].

Using this approach, we present for the first time a biologically constrained whole brain model of larval zebrafish at cellular resolution. The biological constraint was incorporated by the inclusion of the zebrafish structural connectome[23] in the weight-update step. As a result, macroscale subnetworks that resembled major anatomical subregions emerged (**Supplementary Figure 1**). These specific partitions agree with converging evidence that suggest a structural[23] and functional[8,33] separation between front and mid-/hind-brain structures. The parameters of the model form a directed weighted graph, which allowed us to quantify PTZ-induced changes to the underlying graph structure using novel methods in network science[24]. Furthermore, measures were taken to prevent overfitting such as sparsity, which allowed us to perform controlled perturbation simulations.

It is important to state that due to incomplete knowledge of the cell type identity of each of the recorded neurons in our experiments, Dale's principle was not adhered to. However, it is becoming increasing well-recognized that neurons in both zebrafish and rodents can co-release multiple transmitters that may have duel inhibitory and excitatory effects[34,35]. Additionally, the "hidden unit" problem[36] emphasizes that underlying the effective connection between any two neurons are all possible routes that physically link the two neurons. Therefore, it is entirely plausible for an excitatory neuron to exert hyperpolarizing influence over another excitatory neuron (i.e. via disynaptic inhibition). Relatedly, recent research has highlighted that causal modeling can inappropriately infer effective connections between correlated neurons despite no physical link[37]. This can be especially concerning for modeling the preseizure brain as increased firing rates trivially increase correlations[38]. However, the putative increase in firing rates induced by PTZ[8] did not significantly affect network synchronization network (**Fig 1E**), hub cutoff threshold, or the average degree of incoming and outgoing hubs (**Figs 3C,D**).

It should be noted that, certain limitations notwithstanding, the presented models were able to capture various properties reported in biology. For example, we observed that perturbation of a single hub neuron in both zebrafish and mouse control models induces a deflection in the global network dynamics[10] that is quickly stabilized (**Figs. 4,7**) putatively due to effective inhibition[39,40]. Additionally, we found heavy-tailed degree distributions of strong excitatory connections for both zebrafish and mouse models (**Figs. 3C,8D**)[10]. Outgoing

hubs were spatially localized to diencephalon and incoming hubs were spatially localized to telencephalon and mesencephalon (**Figs. 3E,F**). Hub neurons remained in the same relative anatomical locations after PTZ bath application, suggesting diencephalon plays an important role in navigating the brain to a seizure-state. It has been reported that the telencephalon is the principal site of seizure initiation[8] and that the optic tectum is a hub during seizure propagation[20]. Our data add to these insights by suggesting that the telencephalon and optic tectum receives feedforward excitatory inputs from the diencephalon during the preseizure state in a speculated "charge-discharge" cycle. Modeling work supports this concept, having shown with a simple Hebbian plasticity rule increased synaptic weight strength in the initiation site following seizure termination[41].

Higher-order hubs in the epileptic brain

One critical feature of epilepsy models is disrupted inhibition[28,42,43]. In non-epileptic tissue, optogenetic modulation of just a small number of PV interneurons is sufficient to increase the spatial spread of evoked activity[44]. Converging evidence demonstrates that high sensitivity to perturbation is a hallmark of preseizure networks. Specifically, using the high potassium seizure model, Chang *et al.* reported unrestrained activity in CA1 when Schafer collaterals were perturbed[13]. Simulations in a large-scale, data-driven dentate gyrus computational model of TLE predicted that perturbation of a population of neurons that included traditional hubs was sufficient to initiate a seizure[11]. Our work expands on these findings by showing that preseizure networks are sensitive to perturbation of just a single hub (**Figs 4,7**) and thus yields a direct experimental prediction.

To deduce the underlying cause of this observation, we investigated cell-cell communication networks before and after breakdown in $GABA_A$ receptor mediated inhibition caused by PTZ application[28]. Specifically, we deployed novel higher-order clustering techniques[24] to identify structured connectivity patterns surrounding hub neurons and to quantify motif conductance (**Figs 5A,B**). Importantly, the MAPPR algorithm[24] identified optimal clusters, which allowed us to directly compare motif conductance between baseline and preseizure networks. While we reported a non-significant increase (~5%) to average outgoing degree in preseizure networks (**Figs 3C,D**), feedforward motif conductance of higher-order clusters surrounding outgoing hubs increased significantly by 50% on average (**Fig 5E**). These 'higher-order hubs' can therefore more readily propagate sustained excitatory activity downstream compared to baseline networks. Critically, the ability for an individual higher-order hub to destabilize networks in the preseizure state is not linked to outgoing degree (**Figs 5F, 6F, 7J**). This shift in perspective – specifically looking at the patterns of connectivity surrounding hubs as opposed to simple edges from hubs - may be important for how we interpret the underlying microscale dynamics from macroscale recordings[9], evaluate the efficacy of anti-epileptic drugs (AEDs)[18], and develop more strategic closed-loop interventions[1–3].

Motifs are a critical feature of the structural[27,29] and functional connectome[29]. It has been hypothesized that the brain maximizes the diversity of functional motifs[29]. This diversity may be related to the phenomenon of criticality, a state marked by scale-invariant neural avalanches which has been reported in zebrafish[45]. Additionally, prior research showed PTZ-induced disruption of excitation/inhibition ("E/I") balance in cortical neural networks caused deviation away from criticality (one neuron activates one neuron) and into the supercritical regime (one neuron activates more than one neuron)[46]. Feedforward motifs include a 'mother' neuron activating two other cells. Therefore, our discovery of higher-order hubs in the preseizure brain networks suggests a potential network-level marker that captures a system's divergence from criticality.

Our findings in the fish brain were remarkably similar to the results from the hippocampal dentate gyrus of chronically epileptic mice. While zebrafish contain similar neuromodulatory circuits compared to mice[17], one key difference is zebrafish do not have a neocortex. Furthermore, acute seizure models lack persistent alterations to the underlying genes, ion channels, synapses, and morphological properties that are present in patients with epilepsy. We addressed both of these issues by modeling dentate gyrus granule cell dynamics in mice with chronic TLE. Epileptogenesis in TLE involves numerous changes to the underlying cytoarchitecture, including loss of hilar interneurons[47] and mossy fiber sprouting[48] that collectively elevate the net excitability of

the network. These changes alone may explain the reduced stability of a neural network, where computational modeling suggests that perturbation of hub neurons can initiate a seizure[11]. However, predicting functional behavior given a structural connectome is not entirely obvious[29,49]. Here, we uncovered the specific higher-order cell-cell effective interactions that emerged in the chronically epileptic brain as a result of epileptogenesis. These interactions held in completely unrelated experimental epilepsy models (PTZ does not induce structural modifications) and in organisms far removed in evolutionary time. Taken together, these data show a previously unrecognized feature of higher-level cell-cell effective communication pattern that may be a hallmark of a pathological brain state.

Methods

EXPERIMENTAL MODELS AND SUBJECT DETAILS

All procedures were approved by the Institutional Animal Care and Use Committee for both Stanford University and Columbia University.

Zebrafish acute seizure model

Zebrafish

Tg(elavl3:H2B-GCaMP6s)[50] fish (7 dpf) bred on a Nacre or Casper background were used for imaging and registration. Zebrafish were mounted dorsal side up in a thin layer of 2.5% low-melting point agarose (Invitrogen) in the lid of a 3 mm petri dish (Fisher), using a sewing needle to position the fish under a stereomicroscope (Leica M80). Fish were group-housed under a 14:10 light:dark cycle until the day of experiments, and were fed with paramecia (Parameciavap) twice daily from 5-6 days post fertilization onward. All testing occurred during the late morning and afternoon.

Experimental timeline and two-photon imaging

Two-photon volumetric imaging was performed using an Olympus FVMPE multiphoton microscope (Olympus Corporation), with a resonant scanner, in either unidirectional or bidirectional scanning mode. We used a 16x objective (0.8 NA; Nikon). Functional brain imaging was performed at 1.2x zoom (1.44 μm/pix) in 15 z-planes (15 μm spacing) at 0.59s/vol (2500 volumes).

Baseline control imaging was performed for 5 minutes followed by 15 mM bath application of pentylenetetrazol (PTZ) to induce spontaneous seizures[21]. Functional imaging continued for an additional 20 minutes. All zebrafish exhibited at least one putative seizure prior to cessation of imaging.

After functional brain imaging, a structural stack was obtained at 1 μm spacing, starting 15 mm above the first z-plane, ending 15 mm below the last z-plane. Images were registered to Z-brain atlas *Tg(elavl3:H2B-RFP)* volume and single-cell functional calcium dynamics were extracted and denoised with CaIMan[51].

Intrahippocampal kainic acid mouse model of chronical temporal lobe epilepsy

Mice

Male transgenic mice were obtained from The Jackson Laboratory (Nestin-CreER^{T2}:016261; ROSA26-CAG-stop^{flox}-tdTomato Ai9:007909) to establish a local breeding colony on a C57BL/6J background. Mice were housed in the vivarium on a 12h light/dark cycle, were housed 3-5 mice per cage, and had access food and water ad libitum. Mice were housed individually during video-EEG monitoring following kainic acid injection. Mature male and female mice (>8 weeks of age) were used for all experiments.

Experimental timeline

Kainic Acid (KA) was injected into the ventral hippocampus to induce the epilepsy model and rAAV(Syn-GCaMP6f) was injected into the dorsal dentate gyrus ipsilateral to KA injection. Shortly after, a chronic imaging

window was implanted over dorsal dentate and an LFP electrode was inserted adjacent to site of KA injection. Following recovery from injection of KA, mice were placed in video-EEG enabled housing where LFP and behavioral activity were continuously recorded to monitor ictogenesis. Three weeks post-KA injection, the video-EEG verified TLE mice were habituated to being head fixed under the two-photon microscope and concurrent Ca2+ imaging and LFP recording was performed. Detailed surgical procedures are reported in[7].

Two-photon imaging

Two-photon imaging of dentate gyrus granule cells was performed using the same set up as[52], at 4 images/second. Approximately 50-100 mW of laser power under the objective was used for excitation (Ti:Sapphire laser, (Chameleon Ultra II, Coherent) tuned to 920 nm), with adjustments in power levels to accommodate varying window clarity. To optimize light transmission, the angle of the mouse's head was adjusted using two goniometers (Edmund Optics, +/- 10-degree range) such that the imaging window was parallel to the objective. A piezoelectric crystal was coupled to the objective (Nikon 40X NIR water-immersion, 0.8 NA, 3.5mm WD), allowing for rapid displacement of the imaging plane in the z-dimension. OASIS[53] was used for denoising. While not being imaged, mice were routinely monitored for interictal and seizure events using a custom continuous video-EEG system previously described[1]. Healthy control mouse data was obtained from[52], included two-photon recording of granule cells from approximately the same location in dentate gyrus as in epileptic mice.

EFFECTIVE CONNECTIVITY MODELING

Modeling neural dynamics in healthy and pathological brains

Zebrafish

The start of the preseizure state was defined as one minute after PTZ bath application. Start of the seizure state was defined as when the mean population calcium signal was three standard deviations above the average signal from baseline control (pre-PTZ application) dynamics. Correlation matrix analysis[54] was deployed to quantify network synchronization. Modeling in zebrafish was performed on baseline control dynamics first, and the best fit model was used as the initial parameter matrix for learning preseizure dynamics. Community detection using Leiden algorithm[55] on learned parameter matrix was used to identify communities with numerous intra-group connections.

Mice

For both control and chronically epileptic mice, calcium dynamics were acquired during a 30-minute epoch. Calcium recordings included artifacts from running and grooming that resulted in prolonged hyper-synchronous events. Therefore, a continuous 3-5 minute time window lacking such events was identified for each mouse and used to model calcium dynamics.

Chaotic Recurrent Neural Networks

Models of cell-cell effective communication were built using chaotic recurrent neural networks (RNN)[22]. Each neuron experimentally imaged was represented as a node in the network and edges represent the effective (causal) influence between pairs of nodes. The governing dynamics of the chaotic RNN are:

$$\tau \frac{dx_i(t)}{dt} = -x_i(t) + g \sum_{j=1}^{N} J_{ij} \varphi\left(x_j(t)\right) + h_i(t)$$

$$z_i(\mathrm{t}) = \sum_{j=1}^{N} J_{ij} \varphi\left(x_j(t)\right)$$

$$\varphi(.) = \tanh(.)$$

$x_i(t)$ is the inferred intracellular current of node *i*. $\varphi(x_i(t))$ represents firing rate. $z_i(\mathrm{t})$ is the estimated calcium signal. τ is the time constant of the system (zebrafish: 1.5 s; mouse: 0.625 s). $h_i(t)$ is uncorrelated white noise sampled from a normal distribution with mean 0 and standard deviation 0.05 (zebrafish) / 0.005 (mouse). *g* is the gain parameter that determines whether there will be chaos in the system (g<1: stable equilibrium; g>1: chaos). We used g=1.25 for both zebrafish and mouse[25,30]. Lastly, *J* is the effective connectivity matrix that represents the parameters of the model. At initiation of learning baseline control dynamics in zebrafish and learning both control and preseizure dynamics in mice, the values of *J* that were not removed after applying a sparsity mask (zebrafish: 0.10; mouse: 0.40) were sampled from a normal distribution with mean 0 and standard deviation $\frac{1}{\sqrt{Np}}$. *N* is the number of nodes and *p* is the sparsity. The models contain $p * N * (N-1)$ parameters. Dynamics were solved using Euler's method (dt=0.25 s).

Reproducing experimental calcium data using FORCE learning

The effective connectivity parameter matrix was optimized to reproduce the experimental calcium data through FORCE learning[26]. This was done through recursive least-squares optimization where at each time point an error signal $e_i(t) = z_i(t) - f_i(t)$ is calculated between node output $z_i(t)$ and experimental calcium trace $f_i(t)$. Given this error, the traditional learning rule is as follows:

$$\Delta J_{ij} = c * e_i(t) * \sum_{k=1}^{N} P_{jk}\varphi(x_k(t))$$

$$c = \frac{1}{1 + \varphi(t)^T P(t)\varphi(t)}$$

$$P(t) = P(t-1) - cP(t-1)\varphi(t)\varphi(t)^T P(t-1)$$

Where *c* is the effective learning rate used for stability and *P(t)* is updated in a recursive fashion at every time point. At initiation, *P(0)* was set to the identify matrix. Learning was performed for 500 epochs for all zebrafish and mouse models, where one epoch is defined as one run of the optimization routine for the duration of the experimental trial. Convergence was assessed by tracking the mean squared reconstruction error between unit activity and experimental data.

Biologically constrained FORCE using zebrafish structural connectome

The zebrafish structural connectome[23] was incorporated into zebrafish FORCE learning as a biological constraint. The structural connectome is a weighted undirected graph between 30 distinct subregions occupying the telencephalon, diencephalon, mesencephalon, and rhombencephalon. The modified weight-update step is:

$$\Delta J_{ij}^{Constrained} = S_{R(i),R(j)} * \Delta J_{ij}$$

where *i,j* are individual nodes (neurons) and $S_{R(i),R(j)}$ is the structural connectivity between subregions *R(i)* and *R(j)*.

DATA ANALYSIS AND QUANTIFICATION

Identifying traditional hub neurons

The optimized effective connectivity parameter matrix was binarized by converting the top 10% of edges to a 1 and converting the remaining edges to a 0. The outgoing and incoming degree was calculated for each neuron. Neurons above the 90th percentile outgoing (incoming) degree score were marked as outgoing (incoming) hubs.

Force-directed graphs

The effective connectivity matrix was visualized using the Barnes-Hut N-body simulation algorithm[56]. Here, each node can be thought of as a repelling particle and the edges between nodes are modeled as attractive springs. The objective of the algorithm is to find an optimal force-directed spatial configuration such that (i.e. net force = 0). The Barnes-Hut algorithm was applied to the binarized parameter matrix after thresholding for strongest connections (see *Identifying traditional hub neurons*) and used to visualize incoming and outgoing hubs connections in zebrafish.

Perturbation simulations and trajectory deviation

To simulate the effect of perturbation on network dynamics, a single hub neuron was 'current clamped' to achieve maximum firing rate (500ms step current). The current clamp perturbation was initiated at 0.2 normalized time, consistent for all zebrafish and mouse models. Synthetic calcium traces were then generated for each neuron before and after perturbation.

The Euclidean distance *d* between the mean calcium signal of network with perturbation and with the mean calcium signal of network without perturbation was calculated.

$$d(x(t), y(t)) = \sqrt{\sum_{i=1}^{T}(x_i - y_i)^2}$$

To compare simulations across control and epileptic networks, trajectory deviation *TD* was calculated as the Euclidean distance normalized by remaining time points left after start of perturbation t_o.

$$TD(x, y) = \frac{d(x, y)}{T - t_o}$$

Quantifying motif conductance of higher-order hubs using local higher-order clustering

Motif-based approximate Personalized PageRank (MAPPR) algorithm[24] was used to identify an optimal higher-order cluster (i.e. minimum motif conductance) surrounding a hub neuron. Given a motif *M*, MAPPR has three key steps.

Constructing motif weighted graph W

The input graph, taken to be the binarized parameter matrix after thresholding for strongest connections (see *Identifying traditional hub neurons*), is transformed into a weighted graph *W* where the weight depends on *M*. Specifically, W_{ij} is the number of instances of *M* containing nodes *i* and *j*.

Compute the approximate personalized PageRank vector

The personalized PageRank (PPR) vector represents the stationary distribution of a modified random walk seeded on a hub node *u.* At each step of the random walk, the random walker is 'teleported' back to the specified seed node with probability 1 – α, where α was set to 0.98. The stationary distribution of this process for a seed node *u* (the PPR vector p_u), will have larger values for nodes "close" to *u*. The stationary distribution is the solution to the following system of equations:

$$(I - \alpha A D^{-1})p_u = (1 - \alpha)e_u$$

Where *I* is the identify matrix, *A* is the adjacency matrix, *D* is the diagonal degree matrix, and e_u is the vector of all 0's except for a 1 in position *u*. The PPR vector p_u can be approximated via $\widetilde{p_u}$ with accuracy ε = 0.0001 such that

$$0 \leq D^{-1}p_u - D^{-1}\widetilde{p_u} \leq \varepsilon$$

Identify higher-order cluster as set with minimal motif conductance

A sweep procedure is used given approximated APPR vector $\widetilde{p_u}$. Nodes are sorted by descending value of the vector $D^{-1}\,\widetilde{p_u}$ and are incorporated one at a time into a growing set X. After a node added to the set, the motif conductance is calculated.

$$\varphi^{M}(X) = \frac{cut_M(X)}{\min\,(vol_M(X), vol_M(X'))}$$

where $vol_M(X)$ is the number of motif endpoints in X, , $vol_M(X')$ is the number of motif endpoints for nodes not in X, and $cut_M(X)$ is the number of instances of *M* that have at least one end point in X. The set with the smallest motif conductance is deemed optimal and returned. For traditional edge-based clustering, step one is skipped, and the edge conductance score is quantified as above but replacing motif instance *M* with simple edges. Only clusters with at least 5 nodes were considered for analysis.

Statistical analysis

Statistics analysis was performed using python *scipy.stats* package. Comparisons involving more than two groups were p-value adjusted using Bonferroni correction. p-values are reported in all figure subpanels except when p<0.001. Statistical significance was set at 0.05. No data points were left out.

Acknowledgements

The authors would like to thank Michael Kunst for access to zebrafish structural connectivity data, members of the Soltesz Lab and Maxwell Collard for helpful discussions. D.H. was supported by Stanford Interdisciplinary Graduate Fellowship in coordination with Stanford Wu Tsai Neurosciences Institute (Anonymous Donor). M.L-B. was supported by NIH K99MH112840. Z.L. was supported by 1F31NS120783-01. S.C.B. was supported by NIH R01NS096976 and NIH R01NS103139. I.S. and A.L. were supported by NIH R01NS094668 and NIH U19NS104590. Models were built on the Texas Advanced Computing Center (TACC) Frontera system.

Author Contributions

D.H., M.L-B., S.C.B., J.L., A.L., K.D., I.S. designed research; M.L-B., F.S., Z.L. collected data; D.H. performed modeling and simulations; D.H, I.R., I.S. analyzed data; D.H., I.S. wrote manuscript.

Declaration of Interests

The authors declare no competing interests related to this work.

Code and data availability

All code was written in python3 and is available at https://github.com/dhadjia1/soltesz-lab-epilepsy-modeling. Data are available upon request.

References

1. Krook-Magnuson, E., Armstrong, C., Oijala, M. & Soltesz, I. On-demand optogenetic control of spontaneous seizures in temporal lobe epilepsy. *Nature Communications* **4**, 1376 (2013).

2. Bui, A. D. *et al.* Dentate gyrus mossy cells control spontaneous convulsive seizures and spatial memory. *Science* **359**, 787–790 (2018).

3. Krook-Magnuson, E. & Soltesz, I. Beyond the hammer and the scalpel: selective circuit control for the epilepsies. *Nature Neuroscience* **18**, 331–338 (2015).

4. Merricks, E. M. *et al.* Single unit action potentials in humans and the effect of seizure activity. *Brain* **138**, 2891–2906 (2015).

5. Truccolo, W. *et al.* Single-neuron dynamics in human focal epilepsy. *Nat Neurosci* **14**, 635–641 (2011).

6. Muldoon, S. F., Soltesz, I. & Cossart, R. Spatially clustered neuronal assemblies comprise the microstructure of synchrony in chronically epileptic networks. *PNAS* **110**, 3567–3572 (2013).

7. Sparks, F., Liao, Z., Li, W., Soltesz, I. & Losonczy, A. *Adult-born granule cells support pathological microcircuits in the chronically epileptic dentate gyrus*. http://biorxiv.org/lookup/doi/10.1101/2020.05.01.072173 (2020) doi:10.1101/2020.05.01.072173.

8. Liu, J. & Baraban, S. C. Network Properties Revealed during Multi-Scale Calcium Imaging of Seizure Activity in Zebrafish. *eNeuro* **6**, (2019).

9. Farrell, J. S., Nguyen, Q.-A. & Soltesz, I. Resolving the Micro-Macro Disconnect to Address Core Features of Seizure Networks. *Neuron* **101**, 1016–1028 (2019).

10. Bonifazi, P. *et al.* GABAergic hub neurons orchestrate synchrony in developing hippocampal networks. *Science* **326**, 1419–1424 (2009).

11. Morgan, R. J. & Soltesz, I. Nonrandom connectivity of the epileptic dentate gyrus predicts a major role for neuronal hubs in seizures. *Proceedings of the National Academy of Sciences* **105**, 6179–6184 (2008).

12. Hester, M. S. & Danzer, S. C. Hippocampal granule cell pathology in epilepsy — A possible structural basis for comorbidities of epilepsy? *Epilepsy & Behavior* **38**, 105–116 (2014).

13. Chang, W.-C. *et al.* Loss of neuronal network resilience precedes seizures and determines the ictogenic nature of interictal synaptic perturbations. *Nature Neuroscience* **21**, 1742–1752 (2018).

14. Kramer, M. A. & Cash, S. S. Epilepsy as a Disorder of Cortical Network Organization. *Neuroscientist* **18**, 360–372 (2012).

15. Jiruska, P. *et al.* Synchronization and desynchronization in epilepsy: controversies and hypotheses. *The Journal of Physiology* **591**, 787–797 (2013).

16. Tomer, R. *et al.* SPED Light Sheet Microscopy: Fast Mapping of Biological System Structure and Function. *Cell* **163**, 1796–1806 (2015).

17. Lovett-Barron, M. *et al.* Ancestral Circuits for the Coordinated Modulation of Brain State. *Cell* **171**, 1411-1423.e17 (2017).

18. Baraban, S. C., Dinday, M. T. & Hortopan, G. A. Drug screening in Scn1a zebrafish mutant identifies clemizole as a potential Dravet syndrome treatment. *Nat Commun* **4**, 2410 (2013).

19. Burrows, D. R. W. *et al.* Imaging epilepsy in larval zebrafish. *Eur J Paediatr Neurol* **24**, 70–80 (2020).

20. Rosch, R. E., Hunter, P. R., Baldeweg, T., Friston, K. J. & Meyer, M. P. Calcium imaging and dynamic causal modelling reveal brain-wide changes in effective connectivity and synaptic dynamics during epileptic seizures. *PLOS Computational Biology* **14**, e1006375 (2018).

21. Baraban, S. C., Taylor, M. R., Castro, P. A. & Baier, H. Pentylenetetrazole induced changes in zebrafish behavior, neural activity and c-fos expression. *Neuroscience* **131**, 759–768 (2005).

22. Sompolinsky, H., Crisanti, A. & Sommers, H. J. Chaos in Random Neural Networks. *Phys. Rev. Lett.* **61**, 259–262 (1988).

23. Kunst, M. *et al.* A Cellular-Resolution Atlas of the Larval Zebrafish Brain. *Neuron* **103**, 21-38.e5 (2019).

24. Yin, H., Benson, A. R., Leskovec, J. & Gleich, D. F. Local Higher-Order Graph Clustering. in *Proceedings of the 23rd ACM SIGKDD International Conference on Knowledge Discovery and Data Mining* 555–564 (Association for Computing Machinery, 2017). doi:10.1145/3097983.3098069.

25. Andalman, A. S. *et al.* Neuronal Dynamics Regulating Brain and Behavioral State Transitions. *Cell* **177**, 970-985.e20 (2019).

26. Sussillo, D. & Abbott, L. F. Generating Coherent Patterns of Activity from Chaotic Neural Networks. *Neuron* **63**, 544–557 (2009).

27. Song, S., Sjöström, P. J., Reigl, M., Nelson, S. & Chklovskii, D. B. Highly Nonrandom Features of Synaptic Connectivity in Local Cortical Circuits. *PLoS Biol* **3**, (2005).

28. Huang, R. Q. *et al.* Pentylenetetrazole-induced inhibition of recombinant gamma-aminobutyric acid type A (GABA(A)) receptors: mechanism and site of action. *J. Pharmacol. Exp. Ther.* **298**, 986–995 (2001).

29. Sporns, O. & Kötter, R. Motifs in Brain Networks. *PLoS Biol* **2**, (2004).

30. Rajan, K., Harvey, C. D. & Tank, D. W. Recurrent Network models of sequence generation and memory. *Neuron* **90**, 128–142 (2016).

31. Li, N., Daie, K., Svoboda, K. & Druckmann, S. Robust neuronal dynamics in premotor cortex during motor planning. *Nature* **532**, 459–464 (2016).

32. Babloyantz, A. & Destexhe, A. Low-dimensional chaos in an instance of epilepsy. *Proc Natl Acad Sci U S A* **83**, 3513–3517 (1986).

33. Ahrens, M. B., Orger, M. B., Robson, D. N., Li, J. M. & Keller, P. J. Whole-brain functional imaging at cellular resolution using light-sheet microscopy. *Nature Methods* **10**, 413–420 (2013).

34. Lovett-Barron, M. *et al.* Multiple convergent hypothalamus–brainstem circuits drive defensive behavior. *Nat Neurosci* **23**, 959–967 (2020).

35. Billwiller, F. *et al.* GABA–glutamate supramammillary neurons control theta and gamma oscillations in the dentate gyrus during paradoxical (REM) sleep. *Brain Struct Funct* (2020) doi:10.1007/s00429-020-02146-y.

36. Brinkman, B. A. W., Rieke, F., Shea-Brown, E. & Buice, M. A. Predicting how and when hidden neurons skew measured synaptic interactions. *PLoS Comput Biol* **14**, (2018).

37. Das, A. & Fiete, I. R. Systematic errors in connectivity inferred from activity in strongly recurrent networks. *Nature Neuroscience* 1–11 (2020) doi:10.1038/s41593-020-0699-2.

38. de la Rocha, J., Doiron, B., Shea-Brown, E., Josić, K. & Reyes, A. Correlation between neural spike trains increases with firing rate. *Nature* **448**, 802–806 (2007).

39. Isaacson, J. S. & Scanziani, M. How inhibition shapes cortical activity. *Neuron* **72**, 231–243 (2011).

40. Murphy, B. K. & Miller, K. D. Balanced Amplification: A New Mechanism of Selective Amplification of Neural Activity Patterns. *Neuron* **61**, 635–648 (2009).

41. Liou, J. *et al.* A model for focal seizure onset, propagation, evolution, and progression. *eLife* **9**, e50927 (2020).

42. Kobayashi, M. & Buckmaster, P. S. Reduced Inhibition of Dentate Granule Cells in a Model of Temporal Lobe Epilepsy. *J. Neurosci.* **23**, 2440–2452 (2003).

43. Korn, S. J., Giacchino, J. L., Chamberlin, N. L. & Dingledine, R. Epileptiform burst activity induced by potassium in the hippocampus and its regulation by GABA-mediated inhibition. *J. Neurophysiol.* **57**, 325–340 (1987).

44. Yang, J.-W. *et al.* Optogenetic Modulation of a Minor Fraction of Parvalbumin-Positive Interneurons Specifically Affects Spatiotemporal Dynamics of Spontaneous and Sensory-Evoked Activity in Mouse Somatosensory Cortex in Vivo. *Cereb. Cortex* **27**, 5784–5803 (2017).

45. Ponce-Alvarez, A., Jouary, A., Privat, M., Deco, G. & Sumbre, G. Whole-Brain Neuronal Activity Displays Crackling Noise Dynamics. *Neuron* **100**, 1446-1459.e6 (2018).

46. Shew, W. L., Yang, H., Petermann, T., Roy, R. & Plenz, D. Neuronal Avalanches Imply Maximum Dynamic Range in Cortical Networks at Criticality. *J. Neurosci.* **29**, 15595–15600 (2009).

47. de Lanerolle, N. C., Kim, J. H., Robbins, R. J. & Spencer, D. D. Hippocampal interneuron loss and plasticity in human temporal lobe epilepsy. *Brain Res.* **495**, 387–395 (1989).

48. Sutula, T., Cascino, G., Cavazos, J., Parada, I. & Ramirez, L. Mossy fiber synaptic reorganization in the epileptic human temporal lobe. *Annals of Neurology* **26**, 321–330 (1989).

49. Marder, E. & Calabrese, R. L. Principles of rhythmic motor pattern generation. *Physiological Reviews* **76**, 687–717 (1996).

50. Freeman, J. *et al.* Mapping brain activity at scale with cluster computing. *Nature Methods* **11**, 941–950 (2014).

51. Giovannucci, A. *et al.* CaImAn an open source tool for scalable calcium imaging data analysis. *eLife* **8**, e38173 (2019).

52. Danielson, N. B. *et al.* Distinct Contribution of Adult-Born Hippocampal Granule Cells to Context Encoding. *Neuron* **90**, 101–112 (2016).

53. Friedrich, J., Zhou, P. & Paninski, L. Fast online deconvolution of calcium imaging data. *PLOS Computational Biology* **13**, e1005423 (2017).

54. Li, X. *et al.* Synchronization measurement of multiple neuronal populations. *Journal of Neurophysiology* **98**, 3341–3348 (2007).

55. Traag, V. A., Waltman, L. & van Eck, N. J. From Louvain to Leiden: guaranteeing well-connected communities. *Scientific Reports* **9**, 5233 (2019).

56. Barnes, J. & Hut, P. A hierarchical O(N log N) force-calculation algorithm. *Nature* **324**, 446–449 (1986).

Figure Legends

Figure 1: Whole brain imaging of larval zebrafish acute seizure model at single-cell resolution

A: Representative z-plane images acquired from whole-brain cellular resolution two-photon microscopy of larval zebrafish before PTZ (baseline; top) application and during PTZ-induced seizure (bottom).

B: Extracted neural somata point cloud. Colors indicate major brain regions. Orange: telencephalon; Green: diencephalon; Blue: mesencephalon; purple: rhombencephalon

C: (top) Population mean calcium signal and (bottom) heatmap of single-cell functional calcium dynamics from neurons extracted in B. PTZ application, seizure initiation, and seizure termination are demarcated by arrows. Imaging was performed for 25 minutes and PTZ was added 5 minutes into the imaging session.

D: Cross-correlation matrices of single-cell calcium dynamics during baseline, preseizure, and seizure epochs.

E: Quantification of network synchrony from correlation matrices in D show that single-cell calcium dynamics during seizure epoch are significantly more synchronized compared to single-cell calcium dynamics in baseline (one-sided paired t-test, p=0.034 after Bonferroni correction) and in preseizure (one-sided paired t-test, p=0.006 after Bonferroni correction) epochs.

F: Single-cell calcium traces over major anatomical regions plotted during baseline and preseizure epochs. Note the differences in vertical scale bars.

Figure 2: Cellular resolution effective connectivity modeling to infer cell-cell communication networks

A: Cellular resolution chaotic recurrent neural network (RNN) with 90% sparsity constraint to prevent overfitting. Each neuron imaged in the larval zebrafish is represented as a node in the RNN. Edges represent parameters of the model and are were optimized with FORCE learning to match experimental calcium data.

B: The zebrafish structural connectome was incorporated as a biological constraint. (Left) Zebrafish macroscale connectivity matrix (S^{Macro}). (Right) Zebrafish microscale connectivity (S^{micro}), which represents the strength of connectivity between the regions in which neurons *i* and *j* occupy.

C: (Learning rule) FORCE learning tunes the weight J_{ij} between neuron i (target) and j (source). The update is proportional the structural connectivity score S^{micro}_{ij}, multiplied by the difference between unit activity of node *i* (black trace) and target Ca^{2+} waveform acquired experimentally (red trace). (Training pipeline) Models converged using the weight update that incorporated the structural connectome. The baseline model was trained on baseline calcium dynamics with an initial random matrix. To map the changes to the underlying microcircuit connectivity resulting from bath wash in of PTZ, the optimized parameters of the baseline model was then used as the seed for training the preseizure model on preseizure calcium dynamics.

D: Representative examples of mean population Ca^{2+} trace and individual Ca^{2+} traces with modeled fits overlaid for baseline (left) and preseizure (right) dynamics. Note the scale bars. P: population mean calcium signal. (Bottom) PCA state-space analysis of experimental (black) and modeled calcium activity (red).

Figure 3: Identification of outgoing and incoming hubs

A: Hub neurons were separated into incoming (numerous and strong postsynaptic inputs) and outgoing (numerous and strong presynaptic outputs).

(B,C): Algorithm for identifying incoming and outgoing hub neurons in parameter matrix optimized though constrained FORCE learning. **B:** The parameters (top) are binarized into a 0-1 graph (bottom) by keeping the top 10% of excitatory weights. Then, the incoming and outgoing degree for each neuron is calculated from the binarized graph. **C:** Baseline and preseizure network degree distributions for outgoing (top) and incoming

(bottom) degree are heavy-tailed, resembling a power-law. A 90% cutoff (vertical lines) was used to identify outgoing and incoming hubs in each network.

D: 90% threshold cutoff as a fraction of nodes in network and percent change of average hub degree as measured from outgoing (top) and incoming (bottom) degree distributions. Neither paramters was statistically significant between baseline and preseizure networks (two-sided unpaired t-test, $p>0.05$).

E: Spatial distribution of incoming and outgoing hubs for baseline and preseizure states. Orange = telencephalon; Green = diencephalon; Blue = mesencephalon; Purple = rhombencephalon.

F: Fraction of incoming (top) and outgoing (bottom) hubs residing in each macroscale brain region for baseline (open circle) and preseizure (open triangle) networks. Incoming hubs were consistently localized to telencephalon and mesencephalon. Outgoing hubs were consistently localized to diencephalon. Baseline and preseizure networks had similar macroscale spatial organization of incoming and outgoing hubs (unpaired t-test, $p>0.05$).

Figure 4: Perturbation of individual outgoing hubs destabilize preseizure networks

A: Control network response to perturbation (black arrows) of a single outgoing hub. (Top) Population mean calcium signal of experimental data (cyan), unperturbed model (blue), and perturbed model simulation (red). (Bottom) PCA analysis reveals little change in network dynamics in response to perturbation.

B: Perturbation of single outgoing hub in preseizure network showing significant changes to network dynamics compared to A.

C: Violin plots show that perturbing individual outgoing hubs (one-sided Mann-Whitney U-test, $p<0.001$) and incoming hubs (one-sided Mann-Whitney U-test, $p<0.001$) in preseizure networks (purple) had significantly higher influence on network dynamics compared to similar simulations in baseline networks (gray).

D: Outgoing hub trajectory deviation distributions in baseline (gray) and preseizure networks (purple) normalized by incoming hub median trajectory deviation score for the respective populations. Perturbation of outgoing hubs in preseizure state has significantly more influence over network dynamics (one-sided Mann-Whitney U-test, $p<0.001$).

E: Median values from (D) were extracted for each fish and plotted, revealing that preseizure networks have significantly reduced resiliency to perturbation of a single outgoing hub (one-sided paired t-test, $p=0.042$).

F,G: Visual representation of connections between outgoing and incoming hubs for baseline (F) and preseizure (G) network after constrained FORCE learning. Graphs were generated using Barnes-Hut algorithm[56]. Gray edges: outgoing hubs (O.H.) to incoming hubs (I.H.); Purple edges: incoming hubs (I.H.) to incoming hubs (I.H.); Golden edges: outgoing hubs (O.H.) to outgoing hubs (O.H.).

H: Toy model of connections between outgoing (green) and incoming (blue) hubs for baseline (top) and preseizure (bottom) networks.

Figure 5: Emergence of higher-order hubs in preseizure brain

A: Higher-order clustering enables identification of a collection of nodes that form rich feedforward connections with a single hub neurons (left). Importantly, we consider this single hub neuron to be a higher-order hub. This approach contrasts to traditional edge clustering, which only considers simple edges (right). Note that different clusters emerge depending on which method is used.

B: Toy model of higher-order clustering (left) and edge clustering (right) (from Yin *et al*, 2017). Edge conductance quantifies the cluster quality by considering the ratio of edges that span between partitions and which reside completely inside the partition. The motif conductance metric measures the same ratio but with

respect to motifs. Intuitively, the higher the conductance, the more easily it is for excitatory activity to propagate downstream.

C: Violin plots of edge conductance (traditional-hubs; left) and feedforward motif conductance (higher-order hubs; right). Both edge (one-sided Mann-Whitney U, $p<0.001$) and feedforward motif conductance (one-sided Mann-Whitney U, $p<0.001$) are higher in preseizure than baseline networks. However, note the differences in range.

D: Edge conductance (one-sided paired t-test, $p=0.011$) and feedforward motif conductance (one-sided paired t-test; $p=0.033$) are significantly increased in preseizure networks across the sample population. Medians from **C** plotted.

E: Percent change of feedforward motif conductance relative to baseline was significantly greater than edge conductance (one-sided paired t-test, $p=0.047$).

F: Scatter plot of feedforward motif conductance versus outgoing degree of higher-order hubs in baseline and preseizure networks reported no significant correlation between the two variables individually or as a group (see inset).

Figure 6: Disconnecting higher-order hubs stabilizes preseizure networks

A: Edge weights of all simple hubs (via edge clustering) and higher-order hubs (via higher-order clustering) outputs were dampened to explore relative importance of simple edges versus edges belonging to feedforward motifs on network dynamics.

B: (Left) Trajectory deviation after dampening edges projecting from simple hubs and higher-order hubs in baseline and preseizure networks. (Right) Trajectory deviation percent change relative to dampening simple hubs outputs.

C: The effect of disconnecting higher-order hubs with the highest conductance versus lowest conductance on preseizure network dynamics was tested.

D: (Top) Trajectory deviation versus fraction of clusters disconnected in the highest conductance and lowest conductance partitions. (Bottom) Number of edges disconnected for each group.

E: Mean calcium signal of high conductance higher-order hubs and the remaining hub population.

F: Outgoing degree cumulative distribution for high conductance higher-order hubs versus remaining hub population. Importantly, high conductance higher-order hubs are not biased towards the highest outgoing degrees.

G: (Left) Mean population calcium signal spectrograms generated from unchanged/connected preseizure network (top), preseizure network with high conductance higher-order hubs disconnected (middle), and difference. (Right) Power density spectrum (PSD) of mean population calcium signal for baseline, connected preseizure (violet), and disconnected preseizure network.

H: (Left) Percent change of signal variance (i.e. total power) in mean population calcium signal measured before and after perturbation of a single hub. (Right) Trajectory deviation percent change.

I: (Top) Mean population calcium signal of disconnected preseizure network before and after perturbation of a single outgoing hub. (Bottom) PCA analysis before and after perturbation.

Figure 7: Higher-order hubs in kainic acid mouse model of chronical temporal lobe epilepsy

A: Experimental setup. Control and chronically epileptic mice were virally injected with GCaMP in dentate gyrus (DG) and imaged with 2p microscope.

B: DG granule cell DF/F for control and chronically epileptic mouse.

C: Models fits of experimentally recorded granule cells from chronically epileptic granule mouse using FORCE learning.

D: Outgoing and incoming degree distributions for modeled control dentate and chronically epileptic dentate networks showing heavy-tailed distributions.

E: Network response to perturbation (black arrows) of a single outgoing hub neuron in a modeled control (left) and chronically epileptic (right) network.

F: Trajectory deviation in response to perturbation of individual outgoing hubs is significantly higher (one-sided Mann-Whitney U-test, $p<0.001$) in control (gray) than chronically epileptic dentate network (purple).

G: Feedforward motif conductance of individual higher-order hubs is significantly higher (one-sided Mann-Whitney U-test, $p<0.001$) in control (gray) than chronically epileptic (purple) dentate network.

H: Feedforward motif conductance is significantly increased in chronically epileptic networks across the sample population (one-sided unpaired t-test, $p=0.0034$).

I: Outgoing degrees and feedforward motif conductance are not significantly correlated.

J: Higher-order hubs with highest feedforward motif conductance values did not have the highest outgoing degrees (one-sided KS-test, $p=0.71$).

K: Disconnecting feedforward edges of higher-order hubs significantly reduced the response of a chronically epileptic dentate network to perturbation, as measured by percent change in global signal variance (one-sided Wilcoxon signed-rank test, $p<0.001$).

L: Population mean calcium dynamics before (blue) and after (red) perturbation of a single hub for fully connected (left) and disconnected (right) chronically epileptic dentate network.

Figure 1

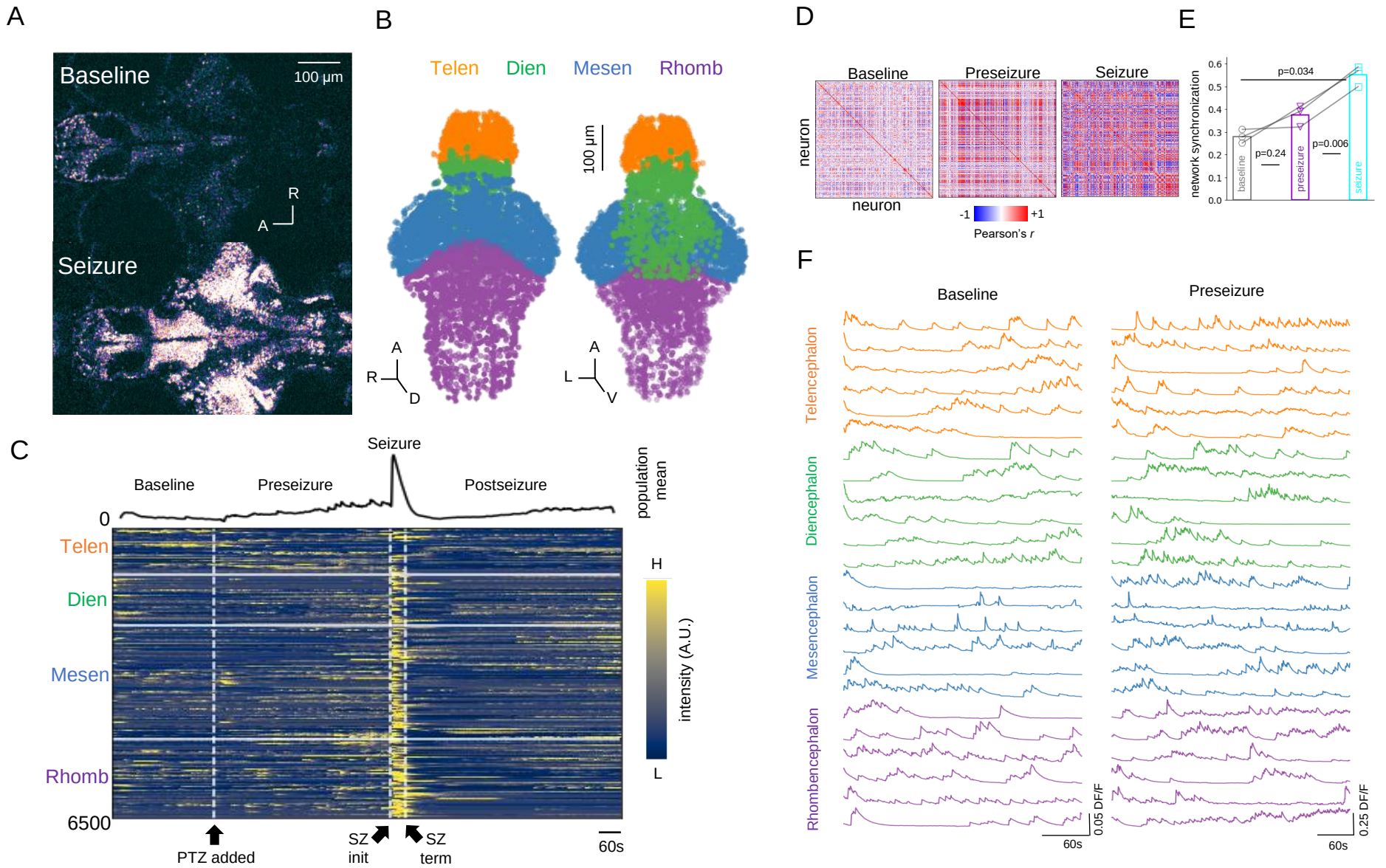
A
Baseline
100 µm
R
A
Seizure
B
Telen
Dien
Mesen
Rhomb
100 µm
A
R
D
A
L
V
C
Seizure
Baseline
Preseizure
Postseizure
population mean
0
Telen
Dien
Mesen
Rhomb
6500
H
L
intensity (A.U.)
PTZ added
SZ init
SZ term
60s
D
Baseline
Preseizure
Seizure
neuron
neuron
-1
+1
Pearson's r
E
network synchronization
p=0.034
p=0.24
p=0.006
baseline
preseizure
seizure
F
Baseline
Preseizure
Telencephalon
Diencephalon
Mesencephalon
Rhombencephalon
0.05 DF/F
60s
0.25 DF/F
60s

Figure 2

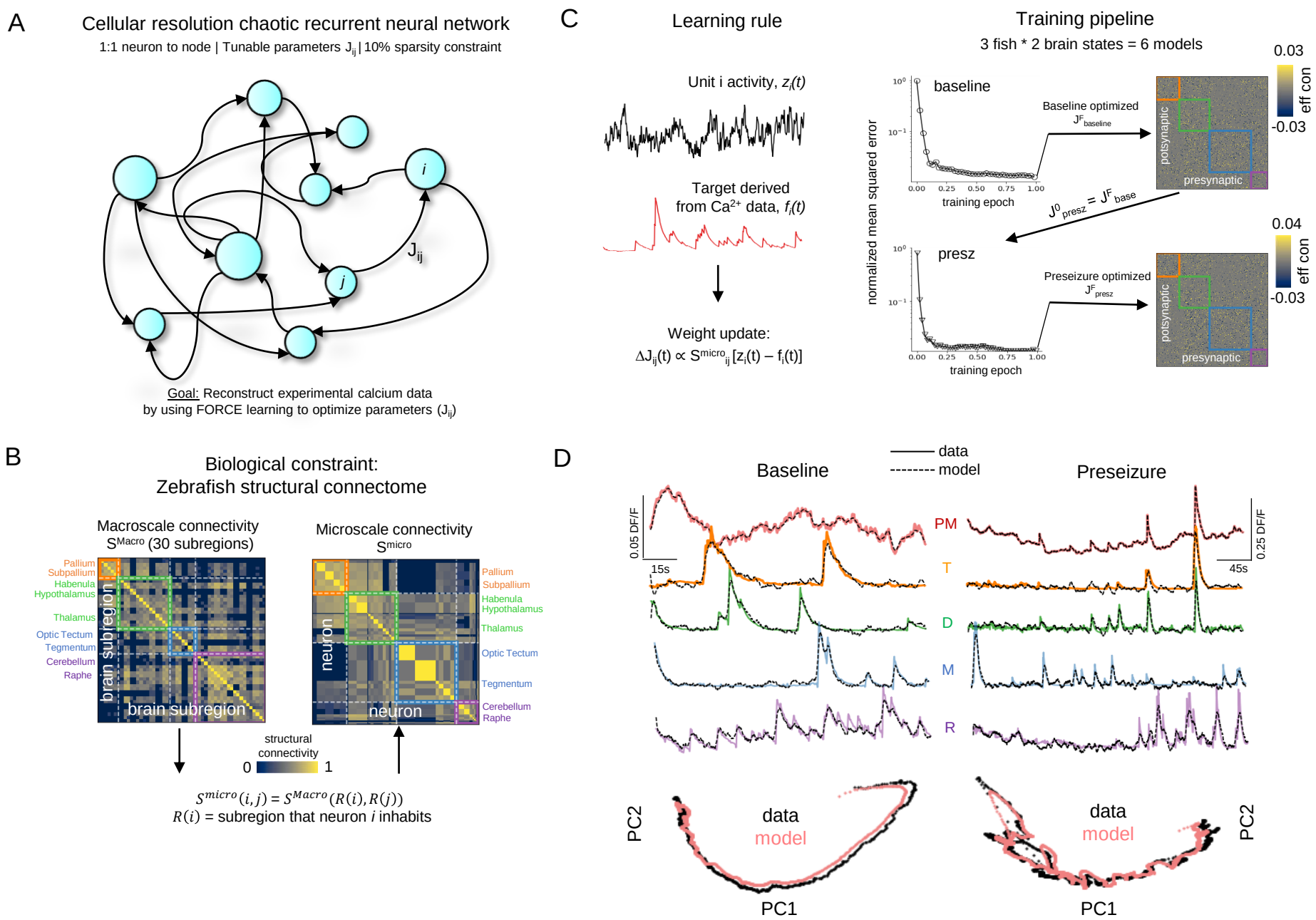
A
Cellular resolution chaotic recurrent neural network
1:1 neuron to node | Tunable parameters J_{ij} | 10% sparsity constraint
i
j
J_{ij}
Goal: Reconstruct experimental calcium data
by using FORCE learning to optimize parameters (J_{ij})
B
Biological constraint:
Zebrafish structural connectome
Macroscale connectivity
S^{Macro} (30 subregions)
Microscale connectivity
S^{micro}
Pallium
Subpallium
Habenula
Hypothalamus
Thalamus
Optic Tectum
Tegmentum
Cerebellum
Raphe
brain subregion
neuron
structural connectivity
0
1
$S^{micro}(i,j) = S^{Macro}(R(i),R(j))$
$R(i)$ = subregion that neuron i inhabits
C
Learning rule
Unit i activity, $z_i(t)$
Target derived from Ca^{2+} data, $f_i(t)$
Weight update:
$\Delta J_{ij}(t) \propto S^{micro}_{ij}[z_i(t) - f_i(t)]$
Training pipeline
3 fish * 2 brain states = 6 models
baseline
Baseline optimized
$J^F_{baseline}$
normalized mean squared error
training epoch
potsynaptic
presynaptic
0.03
-0.03
eff con
$J^0_{presz} = J^F_{base}$
presz
Preseizure optimized
J^F_{presz}
0.04
-0.03
D
data
model
Baseline
Preseizure
0.05 DF/F
15s
0.25 DF/F
45s
PM
T
D
M
R
PC2
PC1
data
model

Figure 3

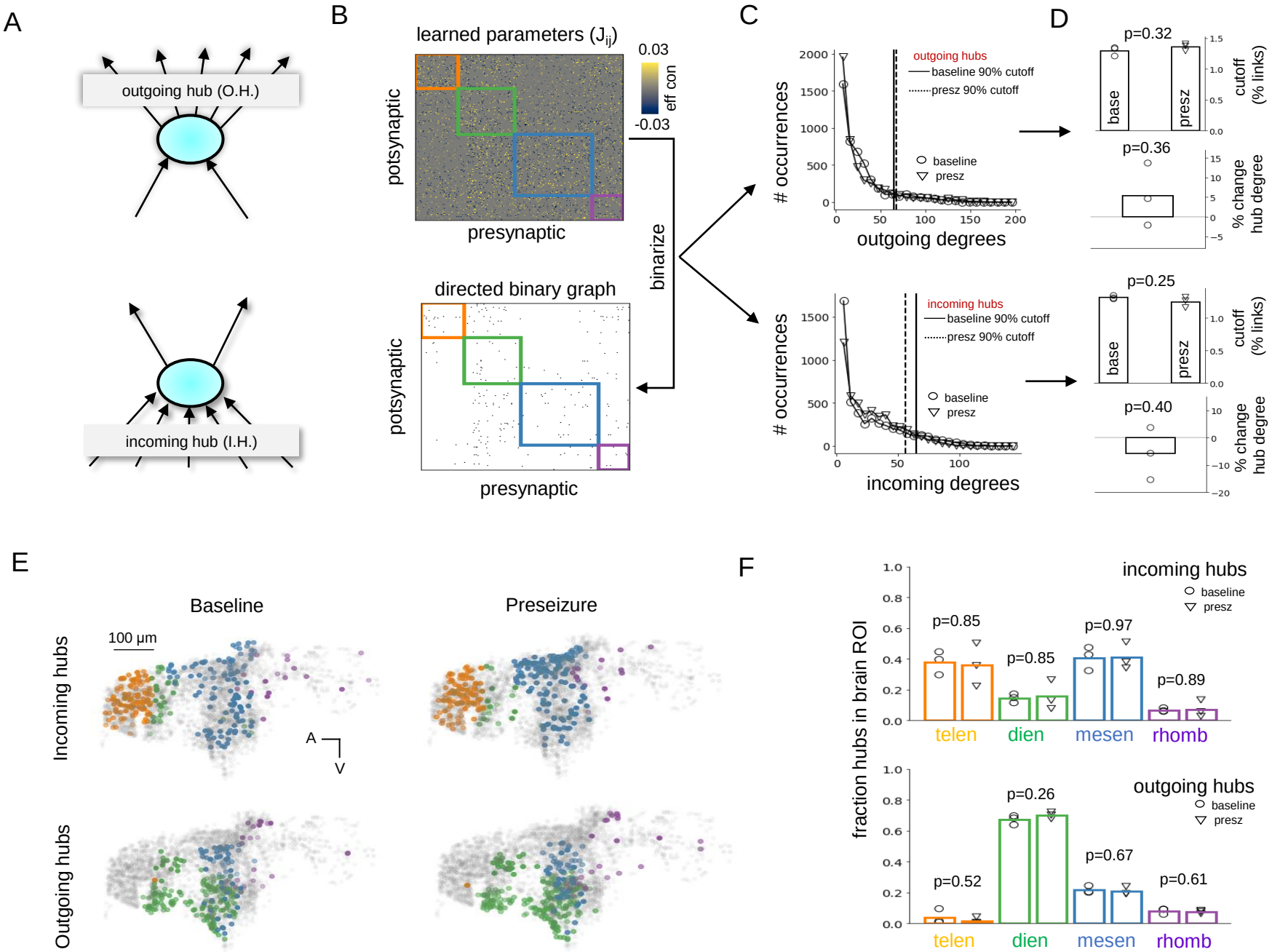
A
outgoing hub (O.H.)
incoming hub (I.H.)
B
learned parameters (J_{ij})
0.03
-0.03
eff con
potsynaptic
presynaptic
binarize
directed binary graph
potsynaptic
presynaptic
C
outgoing hubs
baseline 90% cutoff
presz 90% cutoff
baseline
presz
occurrences
outgoing degrees
incoming hubs
baseline 90% cutoff
presz 90% cutoff
baseline
presz
occurrences
incoming degrees
D
p=0.32
base
presz
cutoff (% links)
p=0.36
% change hub degree
p=0.25
base
presz
cutoff (% links)
p=0.40
% change hub degree
E
Baseline
Preseizure
Incoming hubs
Outgoing hubs
100 µm
A
V
F
incoming hubs
baseline
presz
p=0.85
p=0.85
p=0.97
p=0.89
telen
dien
mesen
rhomb
fraction hubs in brain ROI
outgoing hubs
baseline
presz
p=0.52
p=0.26
p=0.67
p=0.61
telen
dien
mesen
rhomb

Figure 4

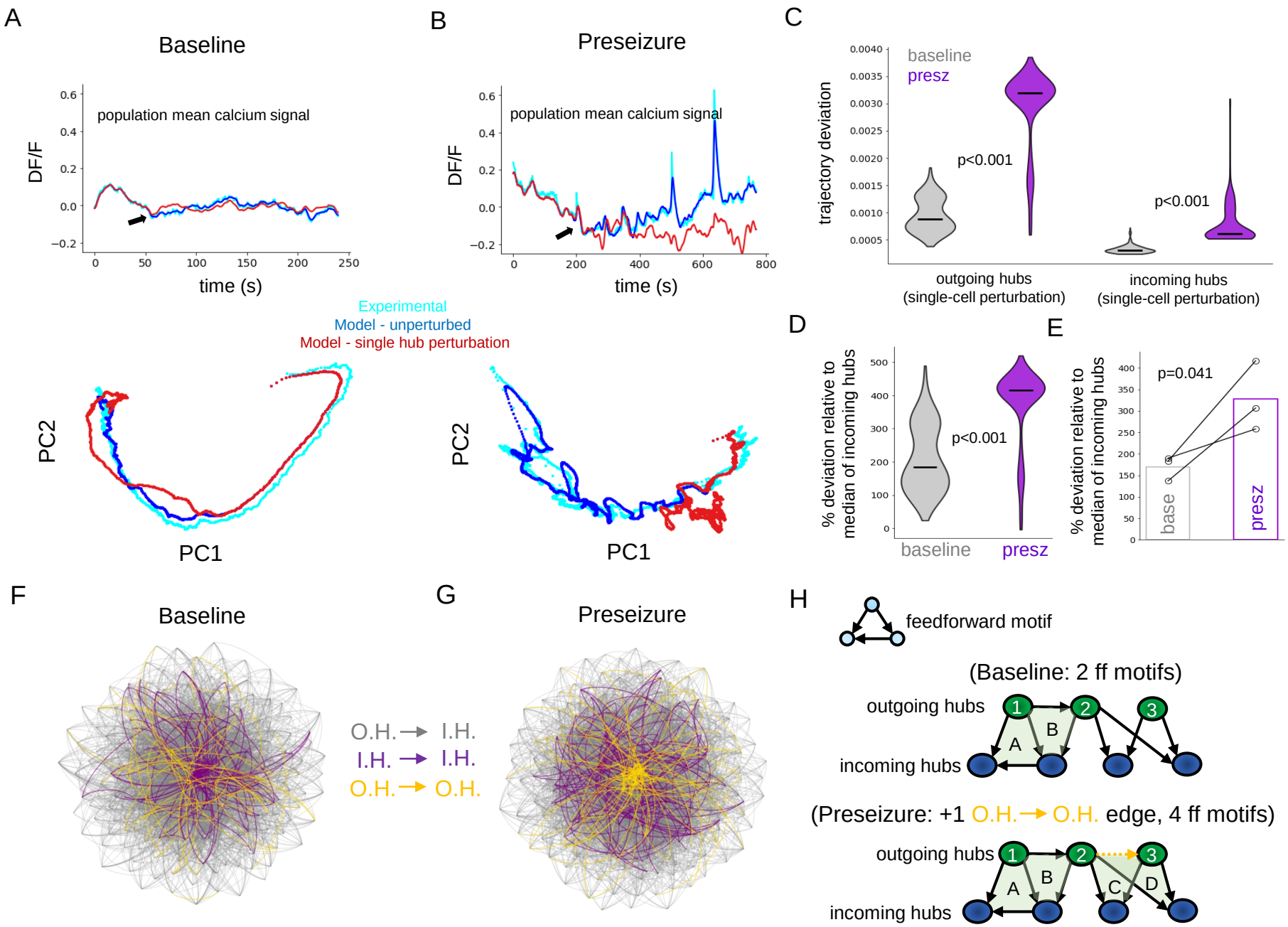
A
Baseline
population mean calcium signal
DF/F
time (s)
B
Preseizure
population mean calcium signal
DF/F
time (s)
C
baseline
presz
trajectory deviation
p<0.001
p<0.001
outgoing hubs
(single-cell perturbation)
incoming hubs
(single-cell perturbation)
Experimental
Model - unperturbed
Model - single hub perturbation
PC2
PC1
PC2
PC1
D
% deviation relative to median of incoming hubs
p<0.001
baseline
presz
E
% deviation relative to median of incoming hubs
p=0.041
base
presz
F
Baseline
G
Preseizure
O.H. → I.H.
I.H. → I.H.
O.H. → O.H.
H
feedforward motif
(Baseline: 2 ff motifs)
outgoing hubs
incoming hubs
A
B
(Preseizure: +1 O.H. → O.H. edge, 4 ff motifs)
outgoing hubs
incoming hubs
A
B
C
D

Figure 5

A

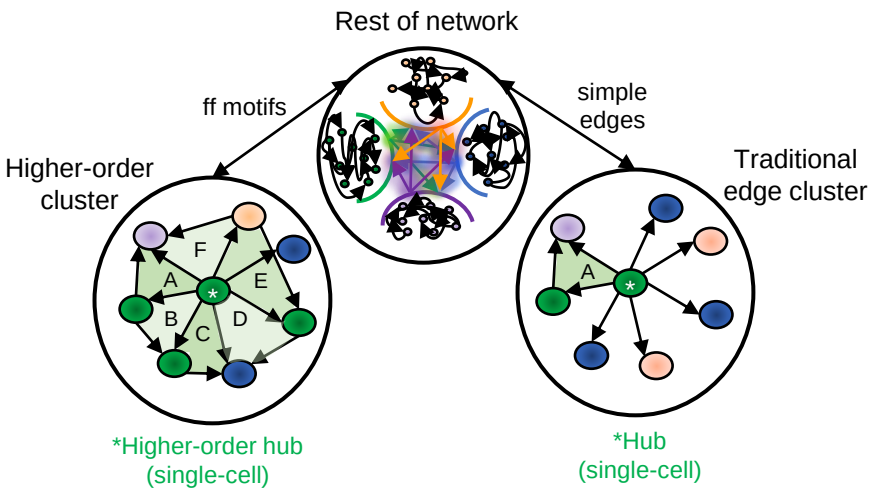

B

Finding higher-order clusters

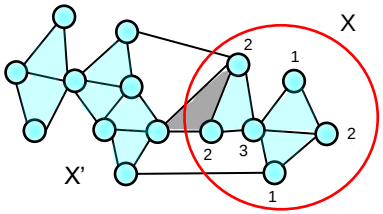

$$\varphi^{M}(X) = \frac{cut_M(X)}{\min(vol_M(X), vol_M(X'))}$$

1 motif cut
11 motif end points
motif conductance = 1/11 = 0.091

Finding traditional edge clusters

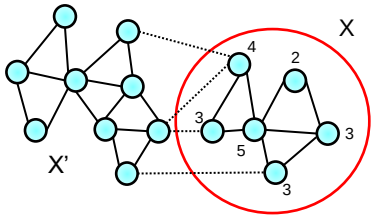

$$\varphi^{edge}(X) = \frac{cut(X)}{\min(vol(X), vol(X'))}$$

4 edges cut
20 edge end points
edge conductance = 4/20 = 0.20

C

local clustering on inferred outgoing hubs

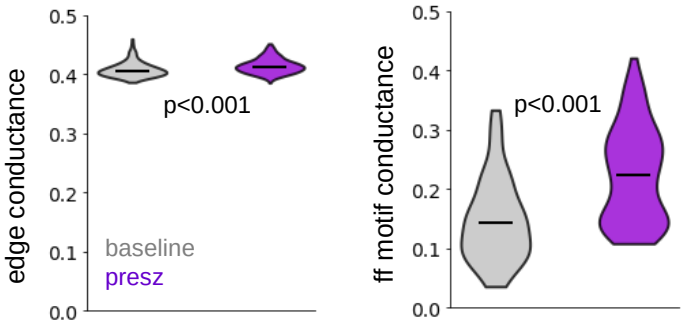

D

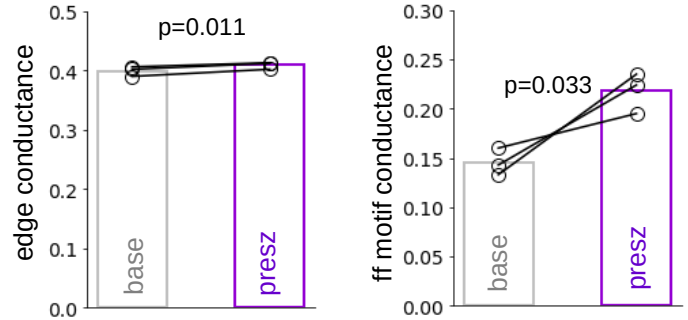

E

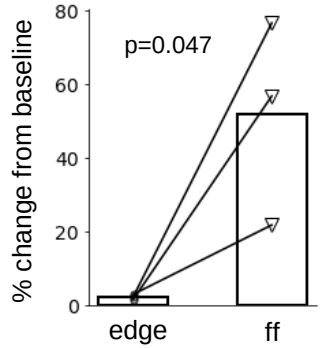

F

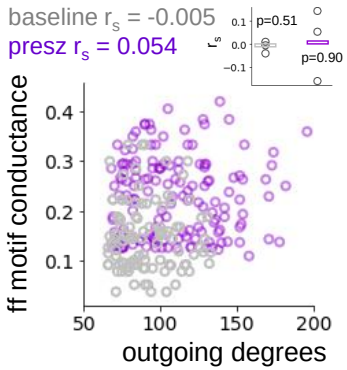

Figure 6

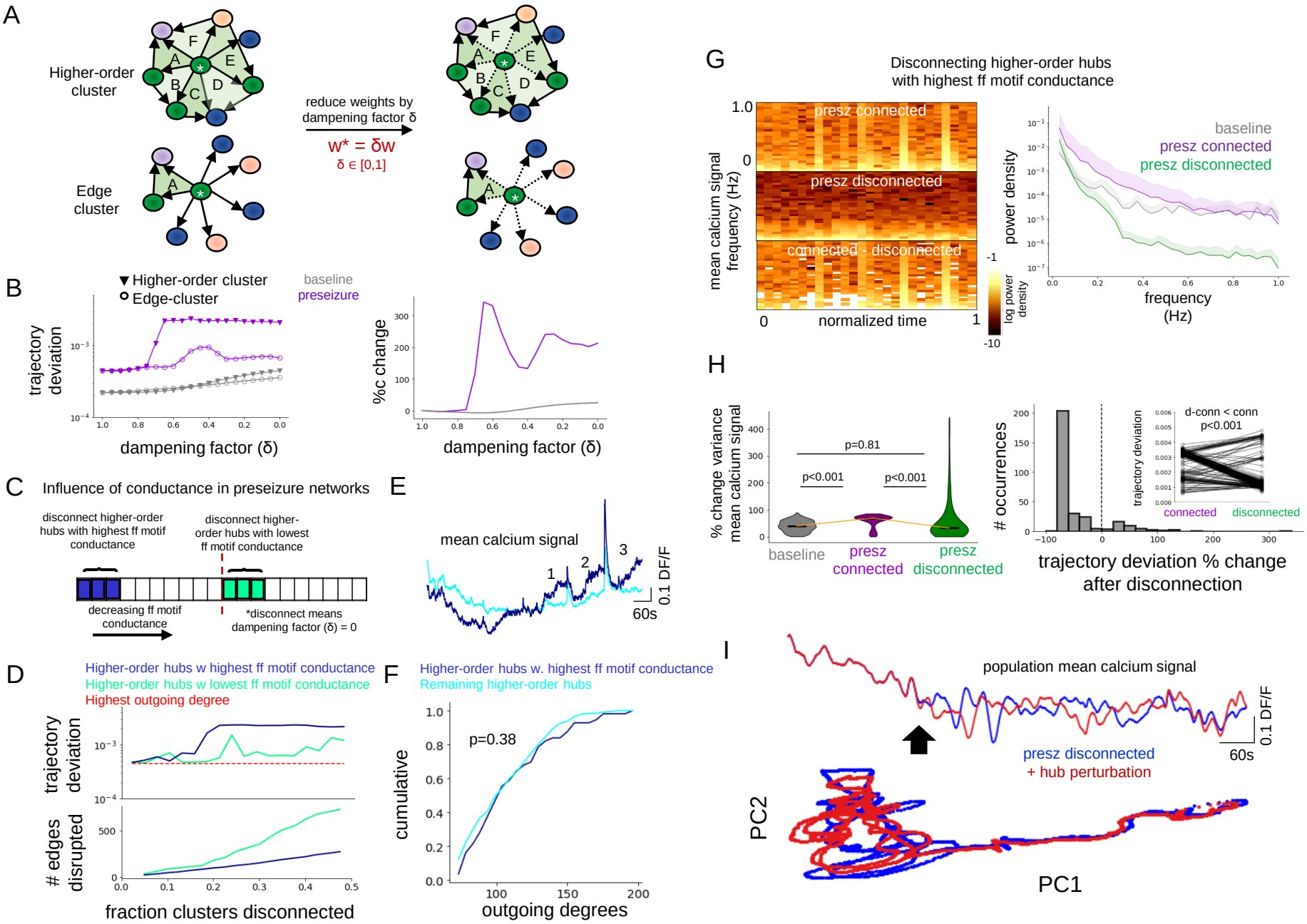
A
Higher-order cluster
Edge cluster
reduce weights by dampening factor δ
w* = δw
δ ∈ [0,1]
B
Higher-order cluster
Edge-cluster
baseline
preseizure
trajectory deviation
dampening factor (δ)
%c change
dampening factor (δ)
C
Influence of conductance in preseizure networks
disconnect higher-order hubs with highest ff motif conductance
disconnect higher-order hubs with lowest ff motif conductance
decreasing ff motif conductance
*disconnect means dampening factor (δ) = 0
D
Higher-order hubs w highest ff motif conductance
Higher-order hubs w lowest ff motif conductance
Highest outgoing degree
trajectory deviation
edges disrupted
fraction clusters disconnected
E
mean calcium signal
0.1 DF/F
60s
F
Higher-order hubs w. highest ff motif conductance
Remaining higher-order hubs
p=0.38
cumulative
outgoing degrees
G
Disconnecting higher-order hubs with highest ff motif conductance
presz connected
presz disconnected
connected - disconnected
mean calcium signal frequency (Hz)
normalized time
log power density
baseline
presz connected
presz disconnected
power density
frequency (Hz)
H
% change variance mean calcium signal
p=0.81
p<0.001
p<0.001
baseline
presz connected
presz disconnected
occurrences
trajectory deviation % change after disconnection
d-conn < conn
p<0.001
trajectory deviation
connected
disconnected
I
population mean calcium signal
0.1 DF/F
60s
presz disconnected
+ hub perturbation
PC2
PC1

Figure 7

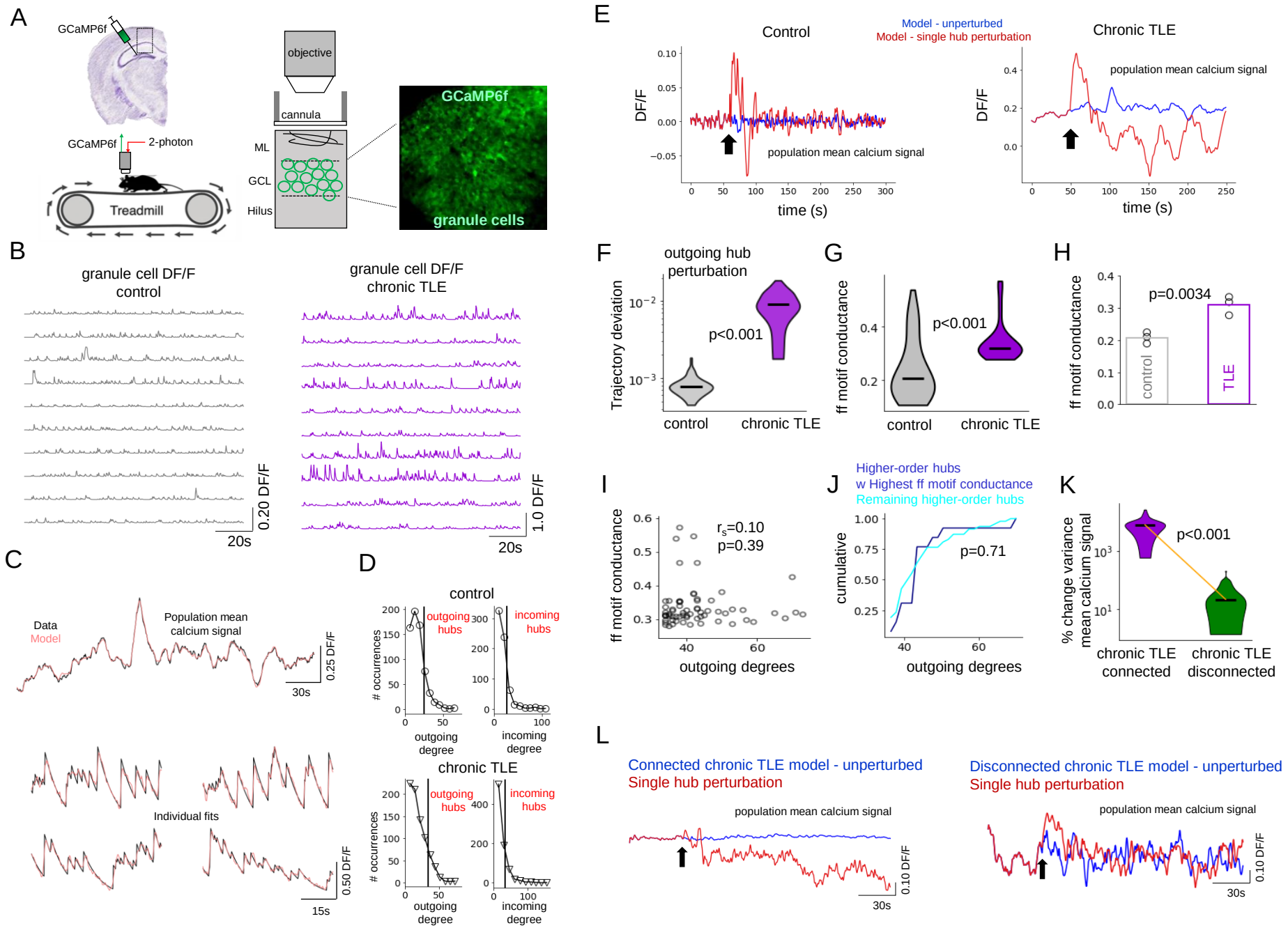
A
GCaMP6f
objective
cannula
GCaMP6f
2-photon
ML
GCL
Hilus
Treadmill
GCaMP6f
granule cells
B
granule cell DF/F
control
granule cell DF/F
chronic TLE
0.20 DF/F
20s
1.0 DF/F
20s
C
Data
Model
Population mean
calcium signal
0.25 DF/F
30s
Individual fits
0.50 DF/F
15s
D
control
outgoing
hubs
incoming
hubs
occurrences
outgoing
degree
incoming
degree
chronic TLE
outgoing
hubs
incoming
hubs
occurrences
outgoing
degree
incoming
degree
E
Control
Model - unperturbed
Model - single hub perturbation
Chronic TLE
DF/F
population mean calcium signal
time (s)
DF/F
population mean calcium signal
time (s)
F
outgoing hub
perturbation
Trajectory deviation
p<0.001
control
chronic TLE
G
ff motif conductance
p<0.001
control
chronic TLE
H
ff motif conductance
p=0.0034
control
TLE
I
ff motif conductance
r_s=0.10
p=0.39
outgoing degrees
J
Higher-order hubs
w Highest ff motif conductance
Remaining higher-order hubs
cumulative
p=0.71
outgoing degrees
K
% change variance
mean calcium signal
p<0.001
chronic TLE
connected
chronic TLE
disconnected
L
Connected chronic TLE model - unperturbed
Single hub perturbation
population mean calcium signal
0.10 DF/F
30s
Disconnected chronic TLE model - unperturbed
Single hub perturbation
population mean calcium signal
0.10 DF/F
30s